Impact of annealing on electrical properties of Cu2ZnSnSe4 absorber layers

Thomas Paul Weiss, Alex Redinger, Germain Rey, Torsten Schwarz, Maria Spies, Oana Cojocura-Mirédin, P.-P. Choi, and Susanne Siebentritt

---

Articles you may be interested in

Research Update: Stable single-phase Zn-rich Cu2ZnSnSe4 through In doping
APL Mater. **4**, 070701 (2016); 10.1063/1.4953435

Semi-empirical device model for Cu2ZnSn(S,Se)4 solar cells
Appl. Phys. Lett. **105**, 033903 (2014); 10.1063/1.4890844

Toward a high Cu2ZnSnS4 solar cell efficiency processed by spray pyrolysis method
J. Renewable Sustainable Energy **5**, 053137 (2013); 10.1063/1.4825253

Atom probe study of Cu2ZnSnSe4 thin-films prepared by co-evaporation and post-deposition annealing
Appl. Phys. Lett. **102**, 042101 (2013); 10.1063/1.4788815

Coevaporation of Cu 2 ZnSnSe 4 thin films
Appl. Phys. Lett. **97**, 092111 (2010); 10.1063/1.3483760

Impact of annealing on electrical properties of Cu₂ZnSnSe₄ absorber layers

Thomas Paul Weiss,[1,a)] Alex Redinger,[1,b)] Germain Rey,[1] Torsten Schwarz,[2,c)]
Maria Spies,[2,d)] Oana Cojocura-Mirédin,[2,c)] P.-P. Choi,[2,e)] and Susanne Siebentritt[1]
[1]Laboratory for Photovoltaics, Physics and Materials Science Research Unit, University of Luxembourg,
L-4422 Belvaux, Luxembourg
[2]Max-Planck-Institut für Eisenforschung GmbH, Max-Planck-Str. 1, 40237 Düsseldorf, Germany

Reported growth processes for kesterite absorber layers generally rely on a sequential process including a final high temperature annealing step. However, the impact and details for this annealing process vary among literature reports and little is known on its impact on electrical properties of the absorber. We used kesterite absorber layers prepared by a high temperature co-evaporation process to explicitly study the impact of two different annealing processes. From electrical characterization it is found that the annealing process incorporates a detrimental deep defect distribution. On the other hand, the doping density could be reduced leading to a better collection and a higher short circuit current density. The activation energy of the doping acceptor was studied with admittance spectroscopy and showed Meyer–Neldel behaviour. This indicates that the entropy significantly contributes to the activation energy. *Published by AIP Publishing*.
[http://dx.doi.org/10.1063/1.4959611]

I. INTRODUCTION

Cu₂ZnSn(S,Se)₄ (CZTSSe) based absorber layers are one of the promising materials for future solar cell technology and benefits from earth abundant metals compared with Cu(In,Ga)Se₂ based solar cells. Currently, the record CZTSSe device has a power conversion efficiency of 12.6%,[1] and recently the pure selenide compound Cu₂ZnSnSe₄ (CZTSe) achieved an efficiency of 11.6%.[2] These record devices rely on a sequential process for the absorber growth,[3] i.e., the growth of a precursor followed by an annealing at elevated temperatures in chalcogenide atmosphere.[4] The details of the reported annealing procedures vary among the groups and little is known on their impact on electrical device characteristics.

In this report we show that the annealing procedure applied for previously reported sequentially processed CZTSe devices[5] is the origin of a deep defect distribution in the absorber layer. Using admittance spectroscopy, we have shown that this deep defect distribution is detrimental for the V_oc.[6] Such a signature of the deep defect distribution observed by admittance spectroscopy is not only measured for devices from University of Luxembourg but also in various other literature reports,[7,8] including a 10.1% efficient

CZTSSe device,[9] and therefore might be of interest for further studies.

Another effect of the annealing is the lowering of the net doping density without altering the composition. Empirically it was found that the net doping density depends on the composition of the sample. Brammertz *et al.* showed that an increasing [Zn]/[Sn] ratio leads to an increasing doping density;[10] while Gunawan *et al.* found that the absorber shows a higher doping with higher Cu content.[11] As will be shown in this manuscript, a change of the doping will not only be evoked by a high temperature annealing but also by a low temperature treatment leading to a better collection and hence a boost of the photogenerated current.

A drawback from the additional heat treatment is the suffering of the open circuit voltage. However, two different heat treatments were applied for this study, which allowed gathering insights into the origin of the V_oc losses. These losses can potentially be prevented depending on process conditions and might be important for sequential processes in general.

II. EXPERIMENTAL

A. Absorber growth

Cu₂ZnSnSe₄ absorber layers were prepared by two different growth techniques: a sequential process and a high temperature co-evaporation process. These two processes are described in the following.

For the sequential process, a Cu-poor precursor was grown by co-evaporating Cu, Zn, Sn, and Se onto an Mo-coated soda lime glass (SLG) held at 320 °C. Subsequently, the precursor was etched in KCN to remove possible Cu_xSe phases.[12] After the etching, the precursor is annealed at 520 °C for 30 min in Se and SnSe atmosphere under 1 mbar

a)Current address: Laboratory for Thin Films and Photovoltaics, Empa, Swiss Federal Laboratories for Materials Science and Technology, Überlandstrasse 129, 8600 Dübendorf, Switzerland, thomas.weiss@empa.ch.
b)Current address: Helmholtz Zentrum Berlin, Department Complex Compound Semiconductor Materials for Photovoltaics, Hahn-Meitner-Platz 1, D-14109 Berlin, Germany.
c)Current address: I. Physikalisches Institut IA, RWTH Aachen University, 52056 Aachen, Germany.
d)Current address: Groupe de Physique des Matriaux, Université et INSA de Rouen, Normandie University, Rouen, France.
e)Current address: Department of Materials Science and Engineering, Korea Advanced Institute of Science and Technology, Daejeon, South Korea.

H$_2$/N$_2$ in a tube furnace to form the absorber layer.[5] This annealing process is referred to as the *high temperature annealing process.*

In the high temperature co-evaporation process the absorber layers were grown at 470 °C by co-evaporating Cu, Zn, Sn, SnSe, and Se onto an Mo-coated SLG substrate either by the two-stage or the multi-stage process (see Ref. 13 for further details). Due to the elevated substrate temperature during growth (compared with the 320 °C for the sequential process), no additional annealing step is needed to form the kesterite absorber layer. To help stabilizing the kesterite phase at the elevated substrate temperature an SnSe evaporation source is added.[14]

Still, in order to study the influence of an additional annealing generally applied for sequentially processed absorbers,[3] two different annealing processes are applied to the high temperature co-evaporated absorbers: the above mentioned *high temperature annealing process* and a *low temperature heat treatment*. For the *low temperature heat treatment* the absorber layers are annealed at 180 °C for 18 h in vacuum with a base pressure of 10^{-8} mbar.

With these additional annealing steps after the high temperature co-evaporation process, four different types of absorbers were fabricated: high temperature co-evaporation (sample A), high temperature co-evaporation plus the *low temperature heat treatment* (sample B and B*), high temperature co-evaporation plus the *high temperature annealing process* (sample C), and a sequential process (sample D). These absorber layers were finished to solar cell devices by a KCN etch followed by a chemical bath deposited CdS buffer layer, magnetron sputtered i-ZnO/Al:ZnO window layer, and an e-beam evaporated Ni/Al grid. The absorber growth during one high temperature co-evaporation run was performed on several substrates simultaneously. Therefore, solar cell devices were also fabricated from the high temperature co-evaporation processes of the samples B, B*, and C (without an additional annealing step). These reference devices are notated as B-ref, B*-ref, and C-ref, respectively, and serve as a direct comparison with respect to the devices, which underwent an additional heat treatment. No reference device of sample D is analysed as the precursor layer grown at 320 °C does not yield a working solar cell. Sample B*-ref was prepared by the same high temperature co-evaporation process as sample B-ref but in a different deposition run. The solar cell yields a worse performance, which is an exception of the process. However, the samples B*-ref and B* are included into the analysis as they help understanding the dominant recombination pathway. A summary over all processes of the analysed solar cell devices is given in Table I.

Before turning to the experimental part of the characterization, several points regarding the absorber growth need to be mentioned. First, it needs to be stressed that the samples B and B* were grown by the multi-stage process, while sample C was grown by the single-stage process.[13] However, for several analysed devices from both processes (single-stage and multi-stage) no significant changes in the device characteristics is observed. Therefore, no difference between these two growth processes is made. Second, the samples were exposed to air between the growth and the additional heat

TABLE I. Summary and overview of the samples which underwent a heat treatment with their corresponding reference cells, denoted with the Appendix *ref*.

Name	Growth (°C)	Anneal. (180 °C)	Anneal. (520 °C)
A	470	…	…
B-ref	470	…	…
B	470	Yes	…
B*-ref	470	…	…
B*	470	Yes	…
C-ref	470	…	…
C	470	…	Yes
D	320	…	Yes

treatment. This might impact the dominant recombination pathway, which will be discussed in Section III B 2.

B. Characterization

Current–voltage (IV) curves were measured with a cold mirror halogen lamp calibrated to 100 mW/cm^2 with a reference Si solar cell. For temperature dependent IV (IVT) measurements the sample was mounted onto a closed cycle helium cryostat allowing for variations in temperature between 320 K and 40 K. The halogen lamp was adjusted to yield the same short circuit current density J$_{sc}$ as measured by the calibrated IV measurement. For admittance spectra, the frequency was varied between 100 Hz and 1 MHz in the same temperature range as for IVT measurements. The characteristics of the admittance spectra do not depend on whether the single-stage or the multi-stage process is used and therefore allows the comparison of these samples. Capacitance–voltage (CV) curves were acquired at low temperatures between +0.7 V and −0.7 V sweeping from positive to negative voltages. After each adjustment of the bias voltage a wait time of 10 s was applied such that it can be assumed that the deep defects are in equilibrium with the bias voltage. The temperature and frequency of the CV measurement was chosen based on the capacitance spectrum obtained from the admittance measurement such that the following two requirements are met. First, the capacitance is not yet influenced by the low temperature step. Second, the measurement is not influenced by the broad capacitance transition at high temperatures, which was previously attributed to a deep defect distribution.[6] These requirements are met for temperatures between 100 K and 200 K (dependent on the individual admittance spectrum) and at a frequency of 1 kHz. The position (temperature and frequency) of the CV measurement is marked in the admittance plots as a open blue circle (see Fig. 4). The doping density was subsequently deduced from the Mott–Schottky plot. The data were fitted in small forward bias to reduce the contributions of deep defects.[15]

External quantum efficiency (EQE) measurements are performed in a home-built setup calibrated with a Si and an InGaAs reference diode. The bandgap was determined by a linear extrapolation of the linear part near the band-edge of the EQE spectrum.
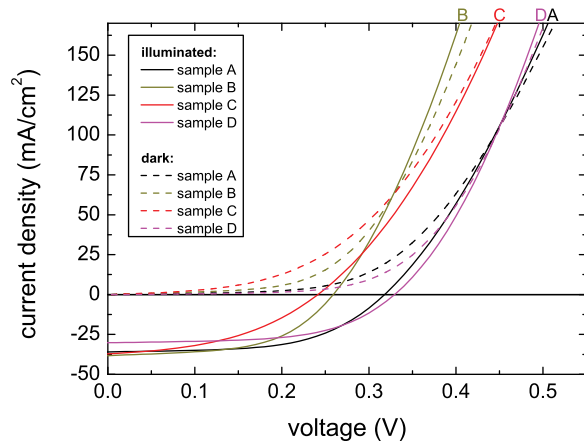
FIG. 1. IV curves of the four samples A, B, C, and D.

Cross-sections from the absorber layers for SEM images were prepared by using a dual-beam focused-ion-beam (FIB). In order to minimize Ga implantation a low energy (5 keV) was used at the final milling step.

Elemental compositions were determined from energy dispersive X-ray spectroscopy (EDX) with an acceleration voltage of 20 kV. Each element was calibrated with elemental standards. Spectra were recorded on spots with an area of approximately $25\,\mu m \times 25\,\mu m$. Several spots were measured to obtain estimates of the compositional inhomogeneity. Besides one of the discussed samples, all samples were homogeneous within EDX error.

III. RESULTS

A. Current-voltage analysis

Fig. 1 shows the current-voltage characteristics of the four samples A, B, C, and D. The solar cell parameters for all devices investigated in this study are listed in Table II and discussed in the following.

When comparing the samples originating directly from the high temperature co-evaporation process (A, B-ref, B*-ref, and C-ref) it is noticeable that the devices B*-ref and C-ref show inferior performance compared with A and B-ref. The performance deficit of the sample B*-ref can be

explained by the strong variation in composition as evident from the standard deviation of the [Zn]/[Sn] ratio deduced from EDX measurement from 10 different spots (see Table II). The performance deficit of sample C-ref is due to a small shunt resistance of only 20 $\Omega\,cm^2$ as deduced from the IV-fit routine.[16] However, this increased shunting will not affect the conclusions drawn when comparing sample C with C-ref and hence the impact of the *high temperature annealing process.*

Applying a heat treatment (either the *low temperature heat treatment* (sample B) or the *high temperature annealing process* (sample C)) to the absorber results in a drop of the V_{oc} while the J_{sc} increases. The increased J_{sc} is a consequence of a reduced doping density leading to a better collection for generation by long wavelength photons as will be shown in Section III D. The deficiency in V_{oc} can be explained by a lowered activation energy of J_0 for the *low temperature heat treatment* and by an additional deep defect distribution for the *high temperature annealing process*. Note that sample D (sequential process) also undergoes the *high temperature annealing process* (and thus exhibiting the deep defect) but having the highest V_{oc} among the devices presented here. The reason for that is the higher bandgap (see Table II) as well as a different depth of the deep defect distribution.[6]

B. Temperature dependent IV

1. Temperature dependence of the photo current and the series resistance

Figure 2(a) shows the temperature dependence of the short circuit current density J_{sc}. A general observation is that the annealed samples show a loss of the photo current when going to low temperatures between 50 K and 150 K as it is evident for the samples B, C, and D. Their reference samples and also sample A do not show this behaviour. Only at temperatures below 70 K the onset of the photo current loss is observed. Fig. 2(b) shows the series resistance with respect to temperature. The series resistance was deduced from the IV curves using the method proposed by Sites and Mauk[17] and Hegedus and Shafarman.[18] The method was applied as long as a reasonable fit in the plot of dV/dJ versus $(1 - GdV/dJ)/(J - GV)$ could be obtained, i.e., not down to the lowest measured temperature. The term of $(1 - GdV/dJ)/(J - GV)$ on the abscissa is

TABLE II. Summary and overview of the samples which underwent a heat treatment with their corresponding reference cells, denoted with the Appendix *ref*. Φ_B and E_g denote the energies for the dominant recombination pathway and the bandgap, respectively. E_{A1} and E_{A2} the deduced activation energies for the corresponding capacitance steps 1 and 2 shown in Fig. 4.

| Name	[Cu]/[Zn] + [Sn]	[Zn]/[Sn]	Eff. (%)	FF (%)	V_{oc} (mV)	J_{sc} (mA/cm^2)	Φ_B (meV)	E_g (meV)	Doping (cm^{-3})	E_{A1} (meV)	E_{A2} (meV)	$E_{A,rs}$ (meV)
A	0.89 ± 0.01^a	0.95 ± 0.01^a	6.4	56.3	318	36.0	821	863	4.6e16	22	n/a	10
B-ref	0.91 ± 0.01^a	0.95 ± 0.01^a	6.5	55.4	325	36.0	835	864	3.6e16	n/a	n/a	20
B	0.89 ± 0.02^a	0.98 ± 0.06^a	5.4	54.4	259	38.3	737	877	6.6e15	121	156	86
B*-ref	0.90 ± 0.02^b	0.95 ± 0.10^b	2.9	48.5	256	23.4	692	861	1.2e17	n/a	n/a	n/a
B*	0.90 ± 0.02^b	0.91 ± 0.04^b	3.8	52.1	247	29.2	734	870	1.0e16	85	…	30
C-ref	0.84 ± 0.01^b	1.03 ± 0.01^b	4.7	44.2	311	34.1	806	869	1.3e17	n/a	n/a	n/a
C	0.83 ± 0.01^b	1.04 ± 0.02^b	3.9	42.9	242	37.2	832	873	1.2e16	55	116	44
D	0.83 ± 0.01^a	1.19 ± 0.03^a	5.7	57.4	329	30.2	843	914	4.3e16	115	164	99

[a] 3 measurements.

[b] 10 measurements.
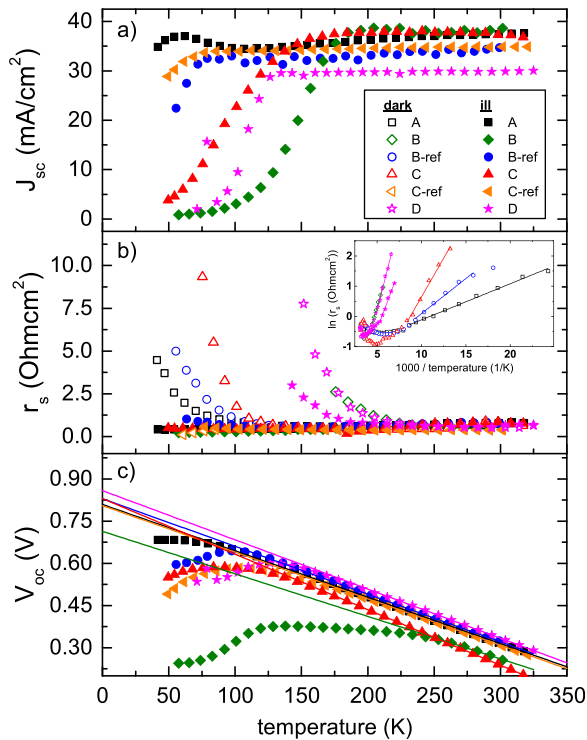
FIG. 2. Temperature dependence of the short circuit current density J_{sc}, the series resistance r_s, and the open circuit voltage V_{oc}. Shown are the four samples A–D as discussed in the text as well as the reference samples B-ref and C-ref. Inset of (b) shows an Arrhenius plot of the series resistance of the annealed samples to highlight its thermal activation.

obtained when taking the shunt conductance G into account.[19] A correlation between the temperature dependence of the series resistance in the dark and the short circuit current can be observed: The J_{sc} decreases with respect to temperature, while the series resistance (in the dark) increases. In fact, the series resistance is thermally activated, as can be seen from the Arrhenius plot shown in the inset of Fig. 2(b). The activation energies $E_{A,rs}$ of the series resistance are listed in Table II.

Under illumination, the series resistance stays rather constant for all samples, except sampled D (precursor grown at 320 °C plus annealing), which shows a thermally activated series resistance even under illumination. A possible origin could be the ZnSe network detected by atom probe tomography (APT)[20] as ZnSe is known to block the current.[21] This ZnSe network was not detected in the high temperature co-evaporated absorbers. Fig. 3 shows polished SEM cross section images for the samples A (co-evaporation, as grown), C (co-evaporation plus *high temperature annealing process*), and D (sequential process). The white patches are ZnSe

grains as detected by EDX and are almost absent in the bulk of the co-evaporated absorber layer. The origin for the accumulation of ZnSe grains only at the back contact for high substrate temperatures during growth (sample A) and under Zn-excess is not yet understood but is in accordance with other co-evaporation studies.[22] In contrast for lower growth temperatures followed by an additional annealing (sample D), the ZnSe forms directly in the bulk of the absorber and apparently does not diffuse (to the back contact). Such a ZnSe distribution is not due to the additional *high temperature annealing process* as it is not observed for sample C (see Fig. 3).

2. Dominant recombination pathway

As mentioned in Section III A a V_{oc} deficit is observed when applying an additional heat treatment. Hence, the temperature dependence of the V_{oc} is studied to deduce the activation energy Φ_B of the dominant recombination pathway. Fig. 2(c) shows the V_{oc} with respect to temperature for samples A, B, B-ref, C, C-ref, and D. Except sample B, all of these devices extrapolate to the same activation energy of roughly 820 ± 20 meV at 0 K, indicating for all of them the same recombination path. Sample B extrapolates to an activation energy of 740 meV and thus yields a significant smaller activation energy of J_0.

Sample B* originates from a worse absorber compared with sample B, as can be seen by the low activation energy of $\Phi_B = 692$ meV for the reference sample B*-ref. After the *low temperature heat treatment* (sample B*) the activation energy is the same as for the sample B. This finding implies the same dominant recombination pathway after the *low temperature heat treatment* (samples B and B*) which is lower than for the other samples. A possible explanation for this observation is the altering of the interface and a potential pinning of the Fermi level.[23] The absorbers were exposed to air before the heat treatment. Thus, oxidation states can form at the interface and could pin the Fermi level. Therefore, it makes sense to get the same pinning position for samples B and B*. In contrast, the high temperature annealing process is carried out in Se and SnSe atmosphere and thus can restore the interface leading to an activation energy for sample C similar to the activation energies obtained for samples A, B-ref, and D (compare Table II). As will be shown in a future publication, the same *low temperature heat treatment* was carried out *in-situ*, i.e., the absorbers were not exposed to air between growth and *low temperature heat treatment*. These samples show an activation energy Φ_B of around
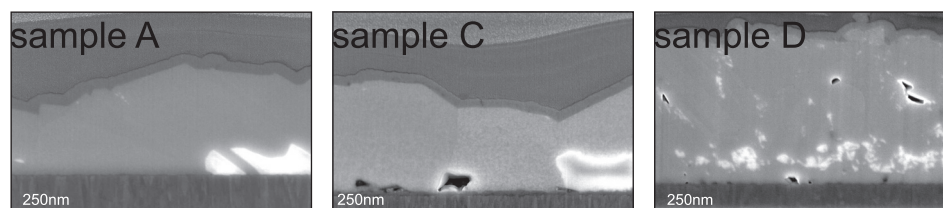

FIG. 3. Cross sectional SEM images for absorbers of type A, C, and D. The white patches are ZnSe as detected by cross sectional EDX mappings. For the high temperature co-evaporation process these ZnSe grains accumulate at the back surface. This distribution does not change for the high temperature annealing process at 520 °C as can be seen for sample C. For the sequentially processed absorbers D the ZnSe is distributed throughout the absorber.

820 meV, which supports the assumption of a degradation due to air exposure.

C. Admittance spectroscopy

1. Impact of the high temperature annealing process

Figure 4 shows the capacitance spectra of the cells A–D. We see several capacitance transitions and these can be attributed as follows: the broad transition at high temperatures covering almost the whole frequency range (marked as number 3) can be attributed to a broad deep defect distribution.[6,24] The broad deep defect distribution was generally observed in our sequentially processed solar cells, where the precursor was grown at 320 °C.[6] Sample A (co-evaporation only) shows this transition to a much lesser extent. However, a number of high temperature co-evaporated samples were measured, where this transition is not apparent at all. The exact process conditions to avoid the occurrence of this defect band are still unknown. Since the deep defect distribution is detected in sample C but neither in the sample C-ref nor in the sample B-ref (admittance spectra not shown), we attribute the significant incorporation of this deep defect distribution to our annealing process.

This defect distribution was quantified by fitting the complete capacitance spectrum with Gaussian defect distributions as described in Ref. 6. With the possibility to quantify that defect distribution, its detrimental effect on V_{oc} could be pointed out.[6] Fitting the capacitance spectrum of

sample C with the method described in Ref. 6 we find a mean defect energy of the deep defect distribution of around 420 meV. The measurement of the bandgap by QE yields a value of $E_g = 873$ meV. Adding the datapoint in the plot of $E_g - qV_{oc}$ versus the mean defect energy (shown in Ref. 6, Fig. 4), it lies on a line with the already existing datapoints. Thus, the low V_{oc} of 242 meV for sample C can be explained by the introduction of the deep defect distribution by the *high temperature annealing process*.

2. Low temperature behaviour

The low temperature capacitance transition in general consists of two overlapping steps (numbered as 1 and 2 in Fig. 4) which correlate with the series resistance.[25,26] Sample A shows this capacitance transition only at very low temperatures below 70 K, roughly in the temperature rage, where the dark series resistance slightly starts to rise (compare Fig. 2). Samples B–D, which all underwent a heat treatment, show this capacitance transition at higher temperatures consistent with the rise of the series resistance (in the dark) in the same temperature range.[25] A comparison of the activation energies for the series resistance and the final capacitance step (E_{A1}) are in good agreement (see Table II) consistent with previous findings.[26] A comparison of these activation energies for a lager number of samples can be found elsewhere.[19]

The high frequency capacitance at low temperatures represents the geometrical capacitance

$$C_{geo} = \frac{\epsilon_R \epsilon_0}{d}, \qquad (1)$$

where the whole absorber acts as a dielectric. d is the thickness of the absorber layer and ϵ_0 and ϵ_R denote the vacuum permittivity and the dielectric constant of the absorber layer, respectively. The thickness d was deduced from SEM cross section images and ϵ_R is assumed between 8 (as reported in Ref. 27) and 10 (a common value for semiconductors[28]). The range of the geometrical capacitance for these values of ϵ_R is calculated according to Eq. (1) and marked as grey bars in Fig. 4. Clearly, the high frequency data at low temperatures matches the calculated geometrical capacitance for the samples B, C, and D. Only sample A differs from the calculated value of C_{geo}, which can be explained by the non zero slope of the capacitance for the highest frequencies and lowest temperatures.

By identifying the final capacitance step with a high frequency value of C_{geo}, a possible explanation is the freeze-out of the doping acceptor as suggested by Gunawan *et al.*[27] Comparing the activation energy E_{A1} for the last capacitance transition we find an activation energy around 20 meV for sample A, while samples after a heat treatment show higher activation energies (see Table II). Generally, for sequentially processed samples activation energies above 70 meV were measured.[26] From these findings and the interpretation of a carrier freeze-out it can be concluded that with the heat treatment the doping defect changes from an acceptor with $E_A \approx 20$ meV to an acceptor with higher activation energies—assuming the absorber to be compensated. In that case
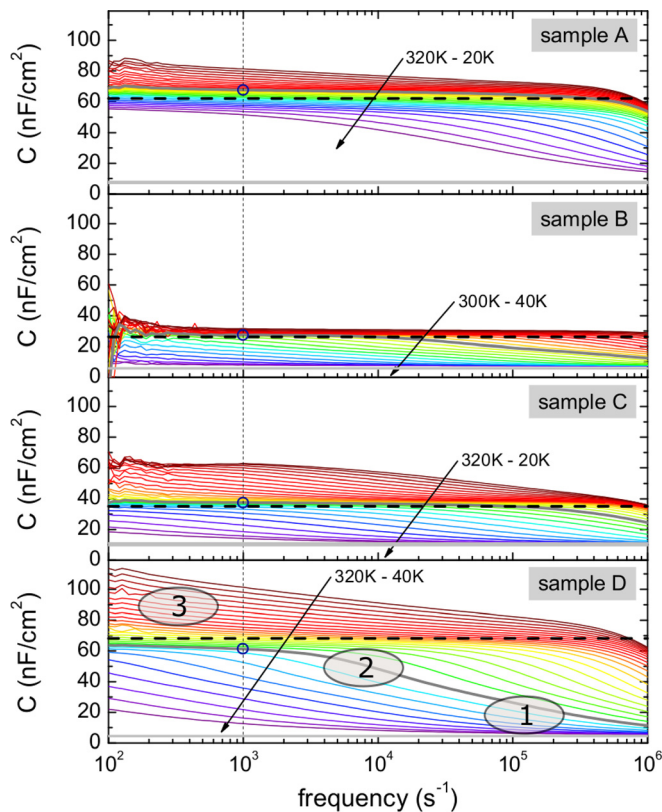

FIG. 4. Capacitance spectra for the samples A–D. The individual capacitance steps are marked for sample D. The dashed black lines correspond to the respective zero bias SCR capacitance values as deduced from Mott–Schottky plots.

E_{A1} denotes the energetic distance from the acceptor level to the valence band maximum. However, this interpretation is revised in Section IV A.

D. Doping density

Another information, which can be deduced from capacitance measurements, is the space charge region (SCR) capacitance. The voltage dependence of the SCR capacitance without deep defects is given by[15]

$$C(V) = \sqrt{\frac{\epsilon_0 \epsilon_R e N_d}{2(V_{bi} - V)}}. \tag{2}$$

Here, N_d denotes the net doping density and V_{bi} is the built-in voltage. Eq. (2) can be rewritten as

$$\frac{1}{C^2} = \frac{2}{\epsilon_0 \epsilon_R e N_d}(V_{bi} - V). \tag{3}$$

Thus, by plotting $1/C^2$ versus the applied bias voltage V (Mott–Schottky plot) the data points should yield a straight line, which can be fitted to obtain V_{bi} and N_d with knowledge of ϵ_R. ϵ_R is assumed to be 10 which is a good estimate for semiconductors.[28] The data are fitted in small forward bias, such that deep defects possibly do not cross the hole quasi Fermi level. In this manner, contributions to the capacitance from deep defects are reduced and the net doping is measured.[15,29] Also reasonable values for the built-in voltage V_{bi} are obtained, which lie in the range of 0.5 V and 0.85 V for the corresponding measurement temperature of the CV profile. The SCR capacitance at 0 bias voltage is then given by

$$C_{\text{SCR}} = \sqrt{\frac{\epsilon_0 \epsilon_R e N_d}{2 V_{bi}}}. \tag{4}$$

The calculated SCR capacitance (Eq. (4)) corresponds to the capacitance just above the low temperature capacitance transition and is marked as a dashed black line in Fig. 4. In samples grown by the high temperature co-evaporation process (sample A) we observe that the SCR capacitance is rather high. Generally, for co-evaporated samples we observe values of the SCR capacitance between 60 nF/cm^2 and 100 nF/cm^2 corresponding to doping densities of the order of 10^{17} cm^{-3}. After the additional *low temperature heat treatment* (sample B) or the *high temperature annealing process* (sample C) we considerably reduced the SCR capacitance and thus the doping

(see Table II and Fig. 4). The doping densities of the devices B* and B*-ref are listed in Table II as well, showing the same trend as B and C with their respective reference devices B-ref and C-ref.

For the sequentially processed samples (like sample D), we measured values of the SCR capacitance between 35 nF/cm^2 and 85 nF/cm^2. These samples were annealed (and cooled) in a tube furnace, where the cooling rate was not controlled. Thus, the time of the heat treatment varied for these samples and therefore could explain the varying doping densities. Additionally, the different micro structure as shown in Fig. 3 could contribute to the varying doping densities.

The consequence of a high doping is a small SCR width. We assume a good collection probability for carriers generated in the SCR (equal to 1), whereas carriers generated in the quasi neutral region (QNR) need to diffuse to the edge of the SCR for field assisted collection. Thus, by increasing the SCR width we can improve the collection, especially for long wavelength photons, which penetrate deeper into the absorber layer. Figure 5 shows a comparison of the external quantum efficiencies (EQEs) for samples with (red dashed curves) and without (black dash dotted curves) the *low temperature heat treatment* (sample B and B-ref, Fig. 5(a)) and the *high temperature annealing process* (sample C and C-ref, Fig. 5(b)). It is evident that the samples show a better collection, where the absorber layer was exposed to a heat treatment. The EQEs show a steeper slope between 1300 nm and 1400 nm pointing to an improved collection.

The bandgap of the devices is determined with the Taucs plot by plotting $(ln(1 - QE)h\nu)^2$ versus the energy $h\nu$ as shown in the insets of Fig. 5. Here, h denotes the Planck's constant and ν the photon frequency. An increase of the bandgap around 10 meV is observed after each additional heat treatment. This change of the bandgap can be attributed to a small amount of ordering in the Cu-Zn planes of the kesterite structure.[30] As it is shown by Rey *et al.* the ordering state of the device can also influence the doping and with that the collection.[31] However, the bandgap can vary by more than 110 meV for the ordered and disordered kesterite[30] and is hence expected to have only a minor effect for these samples.

E. Composition

A change of doping density with composition has been reported by Brammertz *et al.*[10] and Gunawan *et al.*[11] We
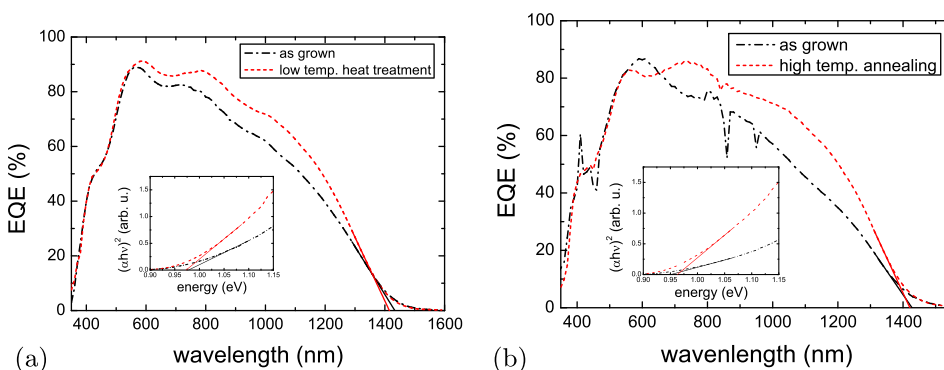

(a)

(b)

FIG. 5. External quantum efficiency before and after the low temperature heat treatment (left) and the high temperature annealing (right). In both cases an increase in the long wavelength response is observed pointing to better collection properties. (a) Low temperature heat treatment and (b) high temperature annealing treatment.

compared the integral composition via EDX at 20 kV before and after the heat treatment and could find a significant change neither in the [Cu]/([Zn] + [Sn]) nor in the [Zn]/[Sn] ratio (see Table II). Therefore, the doping density was changed without changing the integral composition of the film.

IV. DISCUSSION

A. Meyer–Neldel (MN) behaviour

Previously, the change of activation energy obtained from admittance spectroscopy after a heat treatment was assigned to a change in the doping defect. This interpretation is based on the dielectric freeze-out of the charge carriers as proposed by Gunawan *et al.*,[32] where the inflection frequency f_t can be written as

$$f_t = \eta_0 \exp\left(-E_A/kT\right). \tag{5}$$

Here, η_0 contains all constants and is only weakly temperature dependent. This weak temperature dependence is neglected compared with the exponential term.

Fig. 6 shows a Meyer–Neldel (MN)[33] plot for various measured samples including the data points for the samples presented here (black squares). Clearly, the data points form a straight line indicating a Meyer–Neldel behaviour. In this case the entropy contribution cannot be neglected and the activation energy in Eq. (5) needs to be interpreted as the change in the Gibbs free energy $\Delta G = \Delta H - T\Delta S$,[34,35] where ΔH and ΔS denote the change in enthalpy and entropy, respectively. A consequence of the MN rule is that the entropy can be written to be proportional to ΔH such that Eq. (5) expresses as[36,37]

$$f_t = \eta_{00} \exp\left(\frac{\Delta H}{kT_{iso}}\right)\exp\left(-\frac{\Delta H}{kT}\right), \tag{6}$$

and thus explains the correlation of η_0 with the activation energy. Note that the Meyer–Neldel rule is generally observed for the emission of carriers from deep trap states.[35,38–40] However, the MN rule should apply as long as the energy barrier ΔH (compare Eq. (6)) is large with respect to the excitation energy (i.e., phonon energy).[37] By fitting
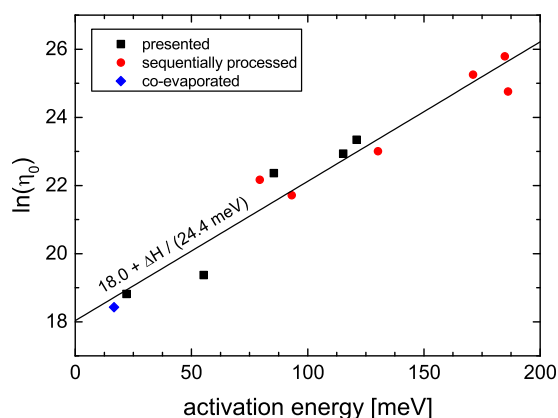

FIG. 6. Meyer–Neldel plot for various measured kesterite solar cell devices.

the data points presented in Fig. 6 an isokinetic temperature T_{iso} of 283 K (= $1/(k \cdot 24.4\,\text{meV})$) is obtained.

From the findings it seems that the heat treatment does not change the doping acceptor as this defect follows the MN rule (Fig. 6), but the activation enthalpy ΔH is changed. The origin of this change in activation enthalpy is currently not yet understood.

V. CONCLUSION

In this manuscript we have prepared absorber layers by a high temperature co-evaporation process and by a sequential process. A major difference between these approaches is the incorporation of a significant amount of ZnSe within the bulk of the absorber layer using the sequential process and could be assigned to the lower growth temperature of the precursor. For the high temperature co-evaporation process the ZnSe accumulates at the back contact and is not changed when applying the *high temperature annealing process*.

To study the influence of a heat treatment on an absorber layer, we applied two different processes to co-evaporated absorber layers: the *low temperature heat treatment* and the *high temperature annealing process*. One consequence of these treatments is a considerably reduced doping density in comparison with their reference samples into a range, which is well suited for solar cell devices. Thus, space charge region width is increased and with that the collection for electrons generated by long wavelength photons as demonstrated by QE spectra.

In conjunction with admittance spectroscopy, the drop of the doping density could be explained by a change of the activation enthalpy of the doping acceptor. However, it was demonstrated that the freeze-out follows a Meyer–Neldel behaviour and thus hints that doping defect remains the same after the heat treatment.

The solar cell performance could not be increased as the V_{oc} suffers from these heat treatments. The origin for the V_{oc} drop depends on the heat treatment and yields valuable information regarding these heat treatments. In the case of the *low temperature heat treatment* it was shown that the activation energy of J_0 is lowered and hence points to a degradation of the interface. Possible reasons could be the exposure to oxygen or a loss of Se as that degradation is not observed for the *high temperature annealing process*. The V_{oc} loss for the *high temperature annealing process* on the other side is due to an incorporation of a deep defect distribution, which was shown to be detrimental to the V_{oc}.[6] This deep defect distribution is generally not observed for the high temperature co-evaporated absorbers (without an heat treatment) and thus can be attributed to the annealing process. Even though similar annealing procedures are generally applied for sequentially processed kesterite absorber layers,[3] this deep defect distribution was never pointed out. Being able to prevent the incorporation of a deep defect distribution during annealing could enhance kesterite based absorber layers by increasing the open circuit voltage.

[1]W. Wang, M. T. Winkler, O. Gunawan, T. Gokmen, T. K. Todorov, Y. Zhu, and D. B. Mitzi, "Device characteristics of CZTSSe thin-film solar cells with 12.6% efficiency," Adv. Energy Mater. **4**, 1301465 (2014).

[2]Y. S. Lee, T. Gershon, O. Gunawan, T. K. Todorov, T. Gokmen, Y. Virgus, and S. Guha, "Cu$_2$ZnSnSe$_4$ thin-film solar cells by thermal co-evaporation with 11.6% efficiency and improved minority carrier diffusion length," Adv. Energy Mater. **5**, 1401372 (2015).

[3]C. M. Fella, Y. E. Romanyuk, and A. N. Tiwari, "Technological status of Cu$_2$ZnSn(S,Se)$_4$ thin film solar cells," Sol. Energy Mater. Sol. Cells **119**, 276–277 (2013).

[4]A. Redinger, D. M. Berg, P. J. Dale, and S. Siebnetritt, "The consequences of Kesterite equilibria for efficient solar cells," J. Am. Chem. Soc. **133**, 3320–3323 (2011).

[5]M. Mousel, T. Schwarz, R. Djemour, T. P. Weiss, J. Sendler, J. C. Malaquias, A. Redinger, O. Cojocaru-Mirédin, P.-P. Choi, and S. Siebentritt, "Cu-rich precursors improve kesterite solar cells," Adv. Energy Mater. **4**, 1300543 (2014).

[6]T. P. Weiss, A. Redinger, D. Regesch, M. Mousel, and S. Siebentritt, "Direct evaluation of defect distributions from admittance spectroscopy," IEEE J. Photovoltaics **4**, 1665–1670 (2014).

[7]K. R. Choudhury, Y. Cao, J. V. Caspar, W. E. Farneth, Q. Guo, A. S. Ionkin, L. K. Johnson, M. Lu, I. Malajovich, D. Radu, H. D. Rosenfeld, and W. Wu, "Characterization and understanding of performance losses in a highly efficient solution-processed CZTSSe thin-film solar cell," in *38th IEEE Photovoltaic Specialists Conference* (IEEE, 2012), pp. 1471–1474.

[8]C. J. Hages, N. J. Carter, J. Moore, S. M. McLeod, C. K. Miskin, C. Joglekar, M. S. Lundstrom, and R. Agrawal, "Device comparison of champion nanocrystal-ink based CZTSSe and CIGSSe solar cells: Capacitance spectroscopy," in 39th IEEE Photovoltaic Specialists Conference (2013).

[9]D. A. R. Barkhouse, O. Gunawan, T. Gokmen, T. K. Todorov, and D. B. Mitzi, "Device characteristics of a 10.1% hydrazine-processed Cu$_2$ZnSn(Se,S)$_4$ solar cell," Prog. Photovoltaics: Res. Appl. **20**, 6–11 (2012).

[10]G. Brammertz, Y. Ren, M. Buffière, S. Mertens, J. Hendrickx, H. Marko, A. E. Zaghi, N. Lenaers, K. Christine, J. Vleugels, M. Meuris, and J. Poortmans, "Electrical characterization of Cu$_2$ZnSnSe$_4$ solar cells from selenization of sputtered metal layers," Thin Solid Films **535**, 348–352 (2013).

[11]O. Gunawan, T. Gokmen, and D. B. Mitzi, "Suns-V$_{OC}$ characteristics of high performance kesterite solar cells," Appl. Phys. Lett. **116**, 084504 (2014).

[12]Y. Hashimoto, N. Kohara, T. Negami, M. Nishitani, and T. Wada, "Surface characterization of chemically treated Cu(In,Ga)Se$_2$ thin films," Jpn. J. Appl. Phys., Part 1 **35**, 4760–4764 (1996).

[13]A. Redinger, J. Sendler, R. Djemour, T. P. Weiss, G. Rey, and S. Siebentritt, "Different bandgaps in Cu$_2$ZnSnSe$_4$: A high temperature coevaporation study," IEEE J. Photovoltaics **5**, 641–648 (2015).

[14]A. Redinger, R. Djemour, T. P. Weiss, J. Sendler, and S. Siebentritt, "Molecular beam epitaxy of Cu$_2$ZnSnSe$_4$ thin films grown on GaAs(001)," in *2013 IEEE 39th Photovoltaic Specialists Conference (PVSC)*, pp. 420–425.

[15]P. Blood and J. W. Orton, *The Electrical Characterization of Semiconductor: Majority Carriers and Electron States* (Academic Press, 1992).

[16]A. R. Burgers, J. A. Eikelboom, A. Schonecker, and W. C. Sinke, "Improved treatment of the strongly varying slope in fitting solar cell i-v curves," in *Conference Record of the 25th IEEE Photovoltaic Specialists Conference* (1996), pp. 569–572.

[17]J. R. Sites and P. H. Mauk, "Diode quality factor determination for thin-film solar cells," Sol. Cells **27**, 411–417 (1989).

[18]S. S. Hegedus and W. N. Shafarman, "Thin-film solar cells: Device measurements and analysis," Prog. Photovoltaics: Res. Appl. **12**, 155–176 (2004).

[19]T. P. Weiss, "Electrical characterization of kesterite thin film absorbers and solar cells," Ph.D. thesis, University of Luxembourg, 2015.

[20]T. Schwarz, O. Mirédin-Cojocaru, P. Choi, M. Mousel, A. Redinger, S. Siebentritt, and D. Raabe, "Atom probe study of Cu$_2$ZnSnSe$_4$ thin-films prepared by co-evaporation and post-deposition annealing," Appl. Phys. Lett. **102**, 042101 (2013).

[21]J. T. Wätjen, J. Engman, M. Edoff, and C. Platzer-Björkman, "Direct evidence of current blocking by ZnSe in Cu$_2$ZnSn (Se$_4$ solar cells," Appl. Phys. Lett. **100**, 173510 (2012).

[22]W.-C. Hsu, I. Repins, C. Beal, C. DeHart, G. Teeter, B. To, Y. Yang, and R. Noufi, "The effect of Zn excess on kesterite solar cells," Sol. Energy Mater. Sol. Cells **113**, 160–164 (2013).

[23]R. Scheer, "Activation energy of heterojunction diode current in the limit of interface recombination," J. Appl. Phys. **105**, 104505 (2009).

[24]M. Burgelman, P. Nollet, and S. Degrave, "Modelling polycrystalline semiconductor solar cells," Thin Solid Films **361–362**, 527–532 (2000).

[25]T. P. Weiss, A. Redinger, J. Luckas, M. Mousel, and S. Siebentritt, "Admittance spectroscopy in kesterite solar cells: Defect signal or circuit response," Appl. Phys. Lett. **102**, 202105 (2013).

[26]T. P. Weiss, A. Redinger, J. Luckas, M. Mousel, and S. Siebentritt, "Role of high series resistance in admittance spectroscopy of kesterite solar cells," in *39th IEEE PVSC* (2013), pp. 3066–3070.

[27]O. Gunawan, T. Gokmen, C. W. Warren, J. D. Cohen, T. K. Todorov, D. A. R. Barkhouse, S. Bag, J. Tang, B. Shin, and D. B. Mitzi, "Electronic properties of the Cu$_2$ZnSn(Se,S)$_4$ absorber layer in solar cells as revealed by admittance spectroscopy and related methods," Appl. Phys. Lett. **100**, 253905 (2012).

[28]K. Seeger, *Semiconductor Physics-Appendix C* (Springer, 2002).

[29]V. Deprédurand, T. Bertram, D. Regesch, B. Henx, and S. Siebentritt, "The influence of se pressure on the electronic properties of CuInSe$_2$ grown under Cu-excess," Appl. Phys. Lett. **105**, 172104 (2014).

[30]G. Rey, A. Redinger, J. Sendler, T. P. Weiss, M. Thevenin, M. Guennou, B. El Adib, and S. Siebentritt, "The band gap of Cu$_2$ZnSnSe$_4$: Effect of order-disorder," Appl. Phys. Lett. **105**, 112106 (2014).

[31]G. Rey, T. P. Weiss, J. Sendler, A. Finger, C. Spindler, F. Werner, M. Melchiorre, M. Hála, M. Guennou, and S. Siebentritt, "Ordering kesterite improve solar cells: A low temperature post-deposition annealing study," Sol. Energy Mater. Sol. Cells **151**(July), 131–138 (2016).

[32]O. Gunawan, T. K. Todorov, and D. B. Mitzi, "Loss mechanisms in hydrazine-processed Cu$_2$ZnSn(Se,S)$_4$ solar cells," Appl. Phys. Lett. **97**, 233506 (2010).

[33]W. Meyer and H. Neldel, "ber die Beziehung zwischen der Energiekonstanten und der Mengenkonstanten a in der Leitwerts-Temperaturformel bei oxydischen Halbleitern," Z. Tech. Phys. **12**, 588 (1937).

[34]O. Engstrom, "Compensation effects at electron traps in semiconductors," Monatsh. Chem. **144**, 73–82 (2013).

[35]S. W. Johnston, R. S. Crandall, and A. Yelon, "Evidence of the Meyer-Neldel rule in InGaAsN alloys and the problem of determining trap capture cross sections," Appl. Phys. Lett. **83**, 908 (2003).

[36]A. Yelon, B. Movaghar, and R. S. Crandall, "Mulit-excitation entropy: Its role in thermodynamic and kinetics," Rep. Prog. Phys. **69**, 1145–1194 (2006).

[37]A. Yelon, B. Movaghar, and H. M. Branz, "Origin and consequences of the compensation (Meyer-Neldel) law," Phys. Rev. B **46**, 12244–12250 (1992).

[38]J. A. M. AbuShama, S. W. Johnston, R. S. Crandall, and R. Noufi, "Meyer-Neldel rule and the influence of entropy on capture cross-section determination in Cu(In,Ga)Se$_2$," Appl. Phys. Lett. **87**, 123502 (2005).

[39]R. S. Crandall, "Analysis of emission rate measurements in a material showing a Meyer-Neldel-rule," MRS Proc. **799**, Z1.6 (2003).

[40]Z. Djebbour, A. Darga, A. M. Dubois, D. Mencaraglia, N. Naghavi, J.-F. Guillemoles, and D. Lincot, "Admittance spectroscopy of cadmium free CIGS solar cells heterointerfaces," Thin Solid Films **511–512**, 320–324 (2006).